Synthesis of core/shell nanocrystals with ordered intermetallic single-atom alloy layers for nitrate electroreduction to ammonia

Qiang Gao
Virginia Tech
Bingqing Yao
National University of Singapore
Hemanth Pillai
Virginia Techu
Wenjie Zang
National University of Singapore
Xue Han
Virginia Tech
Yuanqi Liu
Virginia Tech
Shen-Wei Yu
University of Virginia https://orcid.org/0000-0001-9368-0807
Zihao Yan
Virginia Tech
Bokki Min
Virginia Tech
Sen Zhang
University of Virginia https://orcid.org/0000-0002-1716-3741
Hua Zhou
Argonne National Laboratory
Lu Ma
Brookhaven National Laboratory
Hongliang Xin
Virginia Tech
Qian He
National University of Singapore
Huiyuan Zhu (**huiyuanz@vt.edu**)
Virginia Tech https://orcid.org/0000-0002-9962-1661

Article

Keywords:

Posted Date: September 23rd, 2022

DOI: https://doi.org/10.21203/rs.3.rs-2049958/v1

Abstract

Structurally ordered intermetallic nanocrystals (NCs) and single-atom catalysts (SACs) are two emerging catalytic motifs for sustainable chemical production and energy conversion. Yet, both have limitations in enhancing performance and expanding the materials design space. For example, intermetallic NCs require high-temperature annealing (> 500 °C) to promote atom rearrangement and *d-d* orbital hybridization, leading to potential aggregation or sintering, while SACs are typically limited by a low metal-atom loading (< 1 wt%) to avoid aggregation of metal atoms. Here, we report a facile, direct solution-phase synthesis of Cu/CuAu core/shell NCs with tunable single-atom alloy (SAA) layers. This synthesis can be extended to other Cu/CuM (M = Pt, Pd) systems, in which M atoms are isolated in the Cu host and can be considered the highest density of single-atom sites. We controlled the density of single-sites and the number of atomic layers and investigated the ligand and strain effects of Cu/CuAu for electrocatalytic nitrate reduction reaction (NO_3RR). The Cu/CuAu densely packed SAAs demonstrated a high selectivity toward NH_3 from NO_3RR with an 85.5% Faradaic efficiency (FE) while maintaining an exceedingly high yield rate of 8.47 mol h^{-1} g^{-1}. This work advances the design of atomically precise catalytic sites by creating a new paradigm of core/shell NCs with SAA atomic layers, opening an avenue for broad catalytic applications in achieving a sustainable energy future.

Full Text

Access to nanoscale multifunctionality and synergistic properties requires the development of heterostructures that assemble nanomaterials with distinctive natures. As an example of heterostructured nanomaterials, well-defined core/shell metal nanocrystals (NCs) create interfaces between chemically and structurally dissimilar materials and demonstrate tailorable, synergistic functionality from a spatially controlled distribution of chemical compositions[1-3]. Those core/shell NCs often exhibit enhanced or even unconventional physicochemical properties and thus provide new opportunities for many energy-related catalytic processes, such as the reactions involved in fuel cells (oxygen reduction reaction and fuel oxidation reactions)[4-6], water splitting cells (hydrogen/oxygen evolution reaction)[7,8], and small molecule transformation schemes (CO_2 reduction)[9,10]. In the ideal scenario, core/shell metal NCs need to be fabricated with a low-cost metal core with precious metal atoms in a thin (≤ 1 nm) shell to enhance atom efficiency and to tune NCs' properties through interfacial electronic and geometric effects[11,12]. In particular, tailoring the thin shell in an ordered intermetallic structure with long-range atomic ordering and strong *d-d* orbital coupling could open up new avenues for improving the catalytic properties of core/shell NCs[13-15]. However, high temperature is involved in the phase transformation, leading to a catastrophic failure in creating such a well-defined, atomic precise structure.

To maximize the atom efficiency of precious metals, developing single-atom catalysts (SACs) has emerged as an effective strategy with the surge of recent interest[16,17]. In contrast to the conventional SACs which suffer from a lack of control of single-atom (SA) loading and SA aggregation due to the Gibbs-Thomson effect[18,19], single-atom alloys (SAAs) with atomically dispersed metal atoms in a host

metal, thermodynamically stabilize SAs while still embracing isolated atom centers and tunable electronic properties for enhanced catalysis[20-22]. Moreover, ordered intermetallic structures can be leveraged to break the continuous metal ensembles, representing a structural motif with the highest density of isolated atoms because only the first nearest neighbor of SA is the host metal[23,24]. For example, in the intermetallic *Pm3m* PdIn, Pd atoms are completely isolated by In atoms[21]. Intermetallic *C2/m* $Al_{13}Fe_4$ contains Fe atoms entirely isolated by Al[25]. Pb-modified intermetallic *P2$_1$3* PtGa with single Pt atoms isolated by Ga at the surface exhibits high stability and selectivity for propane dehydrogenation[26]. Thus, one can envision that core/shell NCs with a low-cost metal core and ordered intermetallic SAA shell represent an innovative structural concept and hold promise for many catalytic applications. Nevertheless, it remains a grand challenge to synthesize the precisely tailored nanoscopic architecture of such a well-defined structure.

Herein, to address this challenge, and as a proof-of-concept, we report a facile, direct solution-phase synthesis of Cu/CuAu core/shell NCs with tunable structurally ordered intermetallic SAA layers. The synthesis is also applicable to other Cu/CuM (M = Pt, Pd) systems. Using monodisperse Cu nanocubes as templates and through a seed-mediated colloidal method, we overcome the kinetic barrier for atom diffusion by creating an additional driving force, i.e., the Kirkendall effect driven by galvanic replacement[27,28], other than thermal energy to promote ordered intermetallic formation, lowering the temperature threshold compatible with organic solvents and ligands. We synthetically controlled the density of SAs and investigated the ligand and strain effects of those Cu/CuAu for electrocatalytic nitrate reduction reaction (NO_3RR). NO_3RR offers a promising NH_3 production route alternative to N_2 reduction because it utilizes NO_3^- pollutants as the nitrogen (N)-source, circumventing the activation of the strong N≡N triple bond[29,30]. When coupled with renewable electricity, NO_3RR represents an environmentally friendly and energy-efficient route for the recirculation of N species into the N-cycle and economy[31,32]. Our Cu/CuAu ordered SAA catalysts demonstrate high selectivity toward NH_3 from NO_3RR with a Faradaic efficiency (FE) of 85.5% at -0.5 V vs. the reversible hydrogen electrode (RHE) and an exceedingly high yield rate of 8.47 mol h^{-1} g^{-1} at -0.6 V vs. RHE. Furthermore, Cu/CuAu ordered SAA exhibits catalytic stability for 20 consecutive electrolysis cycles. Density functional theory (DFT) calculations, strain analysis from high-angle annular dark-field (HAADF) scanning transmission electron microscopy (STEM), and *operando* differential electrochemical mass spectrometry (DEMS) suggest that the high activity of the Cu/CuAu catalysts can be attributed to the {001}-oriented Cu site ensemble strengthening the $*NO_3$ binding due to an upshift in the *d*-center of surface Cu atoms while weakening the *N anchoring due to strong repulsive interactions from a subsurface Au ligand or surface Au single atom.

Results

Synthesis and characterization of core/shell Cu/CuAu SAA nanocubes. We tackled the synthesis of precisely controlled deposition of Au SAs and ordered intermetallic CuAu on Cu nanocubes (denoted as Cu/CuAu SAA and Cu/CuAu ordered SAA, respectively) through a facile seed-mediated method, as

illustrated schematically in **Fig. 1**. Firstly, uniform Cu nanocubes with an edge length of 40 nm ± 3 nm were synthesized by a modified method reported previously (**Supplementary Fig. S1**)[33]. A controlled amount of $HAuCl_4$ in oleylamine was then dropwise injected into the solution and incubated for 30 min (**Methods**). The galvanic replacement between the metallic Cu and Au^{3+} induced the Kirkendall effect, promoting atom interdiffusion and rearrangement. The success of our synthesis relies on the dropwise injection of the Au precursor at elevated temperature, which allows Au atoms to instantaneously spread across the Cu surface, resulting in the formation of well-dispersed Au SA on Cu nanocubes. The amount of Au precursor injected plays a crucial role in determining the density of Au SAs, shell thickness, and structure of Au SAA on Cu. The morphology and structure of the particles were then confirmed by transmission electron microscopy (TEM) bright field (BF) and HAADF-STEM imaging, as shown in **Fig. 2**. The as-synthesized Cu/CuAu SAA with ~3.7wt% Au contains nanocubes with a uniform size of 44 nm ± 4 nm (**Fig. 2a**). Zoomed views of an individual Cu/CuAu SAA particle (**Fig. 2b-2c**) show atomic planes with a *d*-spacing of ~0.36 nm in the particle core, corresponding to the (100) planes of the face-centered cubic (*fcc*) Cu structure (ICSD #15985). The atomically dispersed Au atoms in Cu matrix on the shell can be directly visualized with a brighter contrast in the HAADF images, indicating the formation of a dilute SAA. The corresponding fast Fourier-transform (FFT) pattern (**Fig. 2d**) of the nanocube in **Fig. 2c** confirmed that the Cu/CuAu dilute SAA has maintained the *fcc* Cu structure. In contrast, Cu/CuAu ordered SAA nanocubes with ~7.5wt% Au and similar particle size as the Cu/CuAu SAA (**Figure 2e-2f**) demonstrate the formation of the tetragonal *P4/mmm* intermetallic structure of CuAu shell that can be directly observed from the HAADF images (**Fig. 2g and Supplementary Fig. S2**) and the superlattice points (red circles) in the corresponding FFT pattern (**Fig. 2h and Supplementary Fig. S3**). The elemental maps of Au and Cu in **Fig. 2i** show that Au elements are homogeneously distributed on the surface of the nanocubes while Cu elements are distributed across the entire nanocubes, which is consistent with the particle morphology with an intermetallic CuAu shell and a Cu core. We emphasize that in such an intermetallic CuAu structure, Au atoms are completely isolated by Cu atoms (**Supplementary Fig. S4)**.

It is also important to note that the CuAu layers form coherent interfaces with the Cu core. Since the bulk CuAu intermetallic phase (ICSD #42574) has a tetragonal structure with lattice parameters (a=b≈2.80Å, c≈3.67Å) larger than that of the Cu, the CuAu layer is compressively strained by the Cu lattice. **Fig. 2g** shows that there are at least two types of epitaxial relationships, namely $[110](001)_{CuAu}//[100](001)_{Cu}$ and $[110](-110)_{CuAu}//[100](001)_{Cu}$. The CuAu layer also developed domain structures that can relax some mismatch strains at the boundaries or defects. Since the strain status of the CuAu layer can significantly affect its catalytic properties[34], strain analysis was carried out using a representative atomic resolution HAADF-STEM image (**Fig. 2j)**, which has a $[110](-110)_{CuAu}//[001](100)_{Cu}$ epitaxy and is a zoomed view of the region highlighted in **Fig. 2f**. The Au-Au spacings along the $[001]_{Cu}$ and the $[100]_{Cu}$ directions are mapped in **Figs. 2k** and **2l**, respectively. The strains relative to the CuAu bulk lattice parameters are plotted in **Fig. 2m**. At the interface (atomic layer #4), the initial strains in both directions are around 8-10%, and the strain gradually decreases moving toward the surface of the particle. Although it may vary from place to place, the data shown in **Figs. 2k-2m** suggest that around 1-3% compressive strain likely remains at the top surface of the CuAu layer. In contrast, in the case of dilute SAA on Cu

nanocubes, the Cu lattice remains largely unchanged, except for some local variations due to the presence of bigger Au atoms (**Supplementary Fig. S5)**.

The powder X-ray diffraction (XRD) pattern of the Cu/CuAu ordered SAA NCs demonstrates diffraction peaks that match well with the Cu *fcc* phase (**Supplementary Fig. S6**). Panalytical's X-ray diffractometer could not detect the signal of the ordered intermetallic CuAu shell due to the thickness of a few atomic layers. Therefore, synchrotron XRD was performed to characterize the crystal structure of Cu/CuAu SAA NCs. As shown in **Fig. 3a**, in addition to those peaks detected in both Cu/CuAu SAA and Cu NCs, an additional peak at 2θ=15.6 was observed, which can be assigned to the (101) peak of *P4/mmm* ordered intermetallic CuAu structure, consistent with our STEM results. Energy-dispersive X-ray spectroscopy (EDX) results (**Supplementary Fig. 7**) show that the Au weight ratio is about 7.8wt% for ordered Cu/CuAu SAA nanocubes, consistent with the results from the inductively coupled plasma optical emission spectrometry (ICP-OES).

The electronic interactions between Au and Cu were investigated via X-ray absorption near-edge spectroscopy (XANES). **Fig. 3b** and inset show the normalized Au L_3-edge XANES spectra of Cu/CuAu SAA, Cu/CuAu ordered SAA nanocubes, and the reference (Au foil). In comparison with the Au foil, the Cu/CuAu SAA, Cu/CuAu ordered SAA nanocubes show a shift of absorption edge to the lower energy, indicating charge transfer from Cu to Au. **Fig. 3c** and **Supplementary Fig. 8-9** present Fourier-transformed Au L_3-edge extended X-ray absorption fine structure (EXAFS) spectrum of the Cu/CuAu SAA, Cu/CuAu ordered SAA nanocubes, and Au foil. In the R space, Cu/CuAu SAA and Cu/CuAu ordered SAA nanocubes exhibit a prominent peak at ~2.27 Å and ~2.23 Å from the Au-Cu bonds, while no typical peaks for Au-Au bonds at a higher R-value (~2.52 Å) appear. In comparison with Au foil, the Cu/CuAu SAA and Cu/CuAu ordered SAA nanocubes exhibit shorter interatomic distance $R_{Au\text{-}Cu(Au)}$ than that of *fcc* Au atoms in Au foil, and the Au-Au bonds are absent in Cu/CuAu SAA and Cu/CuAu ordered SAA nanocubes. These results confirm that the Au atoms in Cu/CuAu SAA and Cu/CuAu ordered SAA nanocubes present in single atomic dispersion. The wavelet transform (WT) of Au L_3-edge EXAFS oscillations was performed and the corresponding contour plots (**Fig. 3d-f)** demonstrate the intensity maxima at ~10.4 $Å^{-1}$ of Au foil that can be attributed to the Au-Au contribution. In contrast, the WT contour plots of Cu/CuAu SAA and Cu/CuAu ordered SAA nanocubes display the maximum intensity at ~7.0 $Å^{-1}$ and ~6.8 $Å^{-1}$, which is associated with the Au-Cu bonding. Taken cumulatively, the above results indicate that the Au sites are atomically dispersed in Cu/CuAu SAA and Cu/CuAu ordered SAA nanocubes. The developed synthetic methods were further extended to precisely control the deposition of ordered intermetallic CuPd on Cu nanocubes (Cu/CuPd ordered SAA) and ordered intermetallic Cu_3Pt on Cu nanocubes (Cu/Cu_3Pt ordered SAA), demonstrating the generality of the synthesis. As shown in **Supplementary Fig. S10a**, the HAADF image demonstrates the formation of an ordered *B2* CuPd intermetallic structure shell on a Cu core, while the Cu/Cu_3Pt shows an ordered $L1_2$ Cu_3Pt intermetallic structure and Pt SAs on the surface (**Supplementary Fig. S10b**).

NO_3RR on core/shell Cu/CuAu SAA catalysts. We recently reported that the ordered intermetallic CuPd structure could break the adsorption-energy scaling limitations of electrocatalytic NO_3RR to NH_3 by engaging the interatomic coupling from the subsurface ligand[35]. We envision that such an effect can be inherited from the ordered intermetallic structure in our core/shell systems with largely improved precious metal atom efficiency. To evaluate the electrocatalytic NO_3RR activities of the Cu/CuAu SAA and Cu/CuAu ordered SAA nanocubes, the catalysts were loaded onto carbon black (Vulcan XC-72R) (**Supplementary Fig. 11**). As a comparison, Cu nanocubes with a size of ~40 nm (**Supplementary Fig. 1**) and Au nanocubes with a size of ~50 nm (**Supplementary Fig. 12**) were synthesized. The polarization curves for NO_3RR obtained with Cu/CuAu SAA, Cu/CuAu ordered SAA nanocubes, Cu nanocubes, and Au nanocubes are shown in **Fig.4a**. The Cu/CuAu ordered SAA nanocubes show an onset potential of 0.26 V vs. RHE, much more positive than that of Cu/CuAu SAA nanocubes (0.20 V), Cu nanocubes (-0.10 V) and Au nanocubes (-0.18 V). The partial current density of NH_3 on Cu/CuAu ordered SAA nanocubes is also higher than that on Cu/CuAu SAA, Cu, and Au nanocubes (**Fig. 4b**). For the hydrogen evolution reaction (HER), Cu/CuAu SAA and Cu/CuAu ordered SAA show slightly higher activities than Cu but lower than Au (**Supplementary Fig. 13)**. The double-layer capacitance (C_{dl}) of the Cu/CuAu ordered SAA nanocubes is calculated to be 4.75 mF cm^{-2}, which is close to those of Cu/CuAu SAA nanocubes (4.91 mF cm^{-2}) and Cu nanocubes (4.95 mF cm^{-2}), due to the similar size of the catalysts (**Supplementary Fig. 14 and 15**). The ECSA-normalized current densities and partial current densities of NH_3 on Cu/CuAu ordered SAA nanocubes are much higher than that on Cu/CuAu SAA nanocubes, Cu nanocubes, and Au nanocubes, demonstrating that the intrinsic activity for NO_3RR toward NH_3 on Cu/CuAu ordered SAA nanocubes is superior to those on Cu/CuAu SAA nanocubes, Cu and Au nanocubes (**Supplementary Fig. 16**).

Chronoamperometry (CA) measurements of catalysts were conducted at different potentials for 1 h in 1 M KOH + 1 M KNO_3 solution (**Supplementary Fig. 17**). Gas chromatography was employed to detect the quantity of the gas product and only very little H_2 was identified from the competing HER. Ion chromatography was used to quantify produced NO_2^- (**Supplementary Fig. 18**), and the colorimetric method using Nessler's reagent (**Supplementary Fig. 19**) was used to quantify produced NH_3. Faradaic efficiency (FE) and NH_3 yield rates of the catalysts are shown in **Fig. 4c** and **4d.** The Cu/CuAu ordered SAA nanocubes show high selectivity toward NH_3 from NO_3RR with a FE of 85.5% at -0.5 V vs. RHE and an exceedingly high yield rate of 8.47 mol h^{-1} g^{-1} at -0.6 V vs. RHE, outperforming most of the reported catalysts (**Supplementary Table 1**).[36-39] The main byproduct of NO_3RR on Cu/CuAu ordered SAA nanocubes is NO_2^-, as detected and quantified by ion chromatography (**Supplementary Fig. 20**)**.** Control experiments were performed at -0.6 V vs. RHE in 1 M KOH solution without KNO_3. As shown in **Supplementary Fig. 21**, almost no NH_3 was detected in the electrolyte. ^{15}N isotope labeling experiments were carried out to further confirm that the produced NH_3 was derived from the feeding nitrate electrolyte. After electrolysis at -0.6 V vs. RHE, no triple coupling peaks representing $^{14}NH_4^+$ were detected in the ^1H

nuclear magnetic resonance (NMR) spectra of the electrolyte, whereas doublet peaks of $^{15}NH_4^+$ were observed (**Fig. 4e**), confirming that the produced NH_3 is originated from the electroreduction of nitrate.

To investigate the origin of the high performance of Cu/CuAu ordered SAA nanocubes, online DEMS was carried out to identify the intermediates and products (**Fig. 4f**). The m/z signals of 30, 17, 16, 15, and 14 that correspond to NO, NH_3, and fragments of NH_3 appeared during continuous three cycles from 0.4 V to -0.8 V vs. RHE. Since NO was detected in the product gas stream, it is considered an important intermediate in the NO_3RR pathway on our catalysts. Moreover, *in-situ* attenuated total reflectance surface-enhanced infrared absorption spectroscopy (ATR-SEIRAS) was also performed to detect the intermediates on Cu/CuAu ordered SAA during the NO_3RR process. The absorption at around 1645 cm^{-1} can be assigned to H-N-H bending of NH_3 or the H-O-H bending of water molecules[40]. The absorption at around 1370 cm^{-1} can be attributed to the adsorption of NO_3^-[41] (**Supplementary Fig. 22**). The absorption at around 1109 cm^{-1} is due to the adsorption of NH_3[40]. The N=N stretching band at ~2010 cm^{-1} did not appear, indicating that N_2H_x is not a likely intermediate of the NO_3RR on Cu/CuAu ordered SAA[42]. The NO_3RR performance on Cu/CuAu ordered SAA nanocubes in a less concentrated KNO_3 solution demonstrated a slightly higher FE toward NH_3 and lower current density and yield than that in 1 M KNO_3 (**Supplementary Fig. 23**). The stability of catalytic NO_3RR performance was evaluated on Cu/CuAu ordered SAA nanocubes by conducting 20 consecutive electrolysis cycles at a fixed potential (**Fig. 4g**). The FE of NH_3 exhibited a negligible decrease in 20 consecutive electrolysis cycles. As shown in **Supplementary Fig. 24**, after 12 h of continuous operation, there is no apparent decrease in the current density.

Computational insights into NO_3RR on Cu/CuAu SAA nanocubes. DFT calculations were performed to gain insights into the high performance of NO_3RR of the Cu/CuAu ordered and dilute SAA nanocubes. The Cu/CuAu ordered SAA was modeled by cutting the Cu-terminated (100) slab from the body-centered tetragonal (bct) *P4/mmm* CuAu, while for the Cu/CuAu SAA we took the Cu(100) surface and replaced a surface Cu atom with an Au atom, as shown in **Fig. 5a**. The Cu-termination is used because of lower surface energy compared to the Au-termination with surface species, e.g., $*NO_3$. Further details on how each system was modeled and additional computational details are shown in the methods section. While various reaction pathways have been suggested previously, we used the reaction pathway from our previous work which is the most thermodynamically favorable pathway on Cu(100)[35]. **Fig. 5b** shows an activity map at 0 V vs RHE using $*NO_3$ and *N binding energies as two reactivity descriptors. The activity is measured based on the maximum free energy barrier along the reaction pathway. The aforementioned surfaces are marked on this activity map (Au is far beyond the energy range, and thus not shown) and the Cu/CuAu ordered SAA nanocubes show the highest activity, attributed to a stronger $*NO_3$ binding and weaker *N binding. Further analysis of the electronic structures shows that the *d*-band center of Cu atoms for the bct CuAu surface is higher than that of other surfaces, therefore leading to stronger binding of $*NO_3$. The up-shift in the *d*-center also increases the hybridization contribution to the *N binding

interaction as predicted by the traditional *d*-band theory. However, the subsurface Au interacts in a primarily repulsive manner because of a full-occupied *d*-band and large *d*-orbital radius, and thus the overall interaction is weaker, leading to a facile removal of N-bonded species. **Fig. 2k** and **Fig. 2i** showed that the CuAu intermetallic surface has a compressive strain (1-3%). To evaluate the effect of the strain on the activity, the CuAu intermetallic with a 2.5 % compressive strain has been plotted to show the predicted activity. It can be seen that the strain slightly strengthens the *N and weakens the *NO_3, resulting in a negligible effect on the activity. Nevertheless, the strained system is predicted to be more active than the dilute SAA and the Cu(100) surfaces, indicating the dominant role of the ligand effect. The characterization of the Cu/CuAu ordered SAA nanocubes suggested that there are also exists (110) surfaces that are unlikely to be active since it binds *NO_3 too weakly (~ -1.50 eV) (**Supplementary Table 2**).

Conclusions

In summary, we designed and synthesized a new catalytic motif: core/shell dilute SAA and ordered SAA, directly in the solution phase without solid-state thermal treatment. The *d*-states hybridization in the ordered CuAu alloy layers strengthened the *NO_3 binding, and the Pauli repulsion from the fully occupied metal *d*-states led to a weaker *N binding. The surface strain on Cu/CuAu ordered SAA exhibited a negligible effect on tuning the adsorption of key NO_3RR intermediates. As a result, the exceptional ammonia selectivity and yield from NO_3RR on these Cu/CuAu ordered SAA catalysts represents remarkable progress in the development of SAA, ordered intermetallic, and core/shell catalysts. This study opens a new avenue for fabricating tunable, high-loading SAA catalysts by a direct solution synthesis for sustainable electrocatalytic reactions.

Methods

Chemicals. Copper(I) bromide (CuBr, 98%), hydrogen tetrachloroaurate(III) trihydrate ($HAuCl_4 \cdot 3H_2O$, 99.9%), Palladium(II) acetylacetonate [$Pd(acac)_2$, 99%], Platinum(II) acetylacetonate [$Pt(acac)_2$, 97%], trioctylphosphine oxide (TOPO, 99%), oleylamine (OAm, 70%), cetyltrimethylammounium bromide (CTAB), L-ascorbic acid (AA), sodium borohydride ($NaBH_4$), potassium nitrate (KNO_3), potassium hydroxide (KOH), acetic acid, sulfuric acid (H SO), hydrogen peroxide (H O_2), dimethyl sulfoxide (DMSO), Nessler's reagent and Nafion (5 wt%) were all purchased from Sigma-Aldrich. Hexane and ethanol were technical grade from Sigma-Aldrich and were used without further purification.

Synthesis of Cu/CuAu SAA and ordered SAA nanocubes. In a typical procedure, 0.2 mmol CuBr, 0.5 mmol TOPO, and 10 mL OAm were added into a 50 mL three-necked flask under stirring. The mixture was heated under N_2 atmosphere to 80°C and kept at this temperature for 30 min. Then the mixture solution was heated to 260°C at a heating rate of 10°C/min and incubated at this temperature for 30 min, generating a reddish solution. After cooling down to 200°C, 0.5 mL or 1 mL 0.01 mmol/mL $HAuCl_4$ OAm solution was dropwise injected into the solution and incubated at this temperature for 30 min. After

cooling down to room temperature, the precipitate was centrifuged and washed three times with hexane and excessive ethanol and dispersed in hexane. Cu/CuPd ordered SAA and Cu/Cu_3Pt ordered SAA were synthesized by similar procedures to the synthesis of Cu/CuAu ordered SAA except that the precursors were changed to $Pd(acac)_2$ and $Pt(acac)_2$.

Synthesis of Cu nanocubes. In a modified procedure[33], 0.2 mmol of CuBr, 0.5 mmol TOPO, and 10 mL OAm were loaded into a 25 mL three-necked flask under stirring. The mixture was heated under N_2 atmosphere to 80°C and kept at this temperature for 30 min. And then the mixture solution was heated to 260°C at a heating rate of 10°C/min and incubated at this temperature for 30 min, generating a reddish solution. After cooling to room temperature, the precipitate was centrifugated and washed three times with excessive ethanol and dispersed in hexane.

Synthesis of Au nanocubes. In a modified procedure[43], 0.25 mL 10 mM $HAuCl_4 \cdot 3H_2O$ aqueous solution was added into 7.5 mL 100 mM CTAB aqueous solution, which was gently mixed by magnetic stirring. Subsequently, 0.60 mL 10 mM of ice-cold freshly prepared $NaBH_4$ aqueous solution was added, followed by magnetic stirring for 2 min. The solution was then left undisturbed at 25°C for 1 h to obtain Au seeds. Then 2.0 mL, 10 mM $HAuCl_4 \cdot 3H_2O$ aqueous solution was added to the mixture containing 16 mL 100 mM CTAB solution and 80 mL of deionized water. Then 9.5 mL 100 mM L-ascorbic acid aqueous solution was added. Finally, 50 μL of the 1 h-aged, diluted Au seed solution (diluted 10 times with deionized water) was added to the solution, which was kept undisturbed for 1 h. The product was collected by centrifugation, washed several times with deionized water, and dispersed in deionized water.

Preparation of carbon-supported catalysts (20% loading). To prepare carbon-supported catalysts, we mixed a hexane dispersion of 20 mg of catalysts with 80 mg activated carbon (Vulcan XC-72R) and sonicated for 2 h. The catalysts were collected by centrifugation, washed three times with excessive ethanol and dried for 8 h in a vacuum oven at 60°C.

Characterization. XRD was performed on a Philips X' Pert PRO SUPER with Cu Kα (λ = 1.54056 Å). XPS was performed on a PHI Versa Probe III scanning XPS microscope using a monochromatic Al K-alpha X-ray source (1486.6 eV). The morphology was characterized by TEM (EM-420). BF and HAADF STEM and X-EDS were conducted on a JEOL ARM 200CF equipped with an Oxford Instrument X-ray Energy Dispersive Spectrometer. The element contents of the Cu/CuAu SAAs were determined by ICP-OES on a SPECTRO GENESIS ICP spectrometer. The colorimetric method with Nessler's reagent on a UV-vis spectrophotometer (Agilent 3500) was used to quantify the produced ammonia. The gas product was quantified by gas chromatography (Agilent 7890B). Ion chromatography (Metrohm Eco IC) was used to quantify the produced nitrite. Liquid products were analyzed by ^1H NMR using DMSO as an internal standard. The X-ray absorption spectra of Au and Cu K-edges were obtained at the beamline 12-BM-B station of the Advanced Photon Source at Argonne National Laboratory. Both Au L_3-edge and Cu K-edge XANES and EXAFS were measured under fluorescence mode by a Vortex ME4 detector. All XAS data analyses were performed with the Athena software package to extract XANES and EXAFS. Synchrotron

XRD data were collected at 20 keV (λ = 0.6199 Å) at beamline 7-BM of NSLS- , Brookhaven National Lab. The distance from detector to the sample was 299.48 mm, calibrated with LaB6. The 2D XRD patterns were integrated with software Dioptas.

Electrochemical Measurements. Electrochemical measurements were performed using a three-electrode system connected to a BioLogic electrochemical workstation. All measurements were performed at room temperature in a gas-tight H-cell separated by an ion-exchange membrane (Nafion 117). Before testing, the Nafion 117 membrane was pretreated in 5% H_2O_2 solution at 80°C for 1 h, then in 0.5 M H_2SO_4 solution at 80°C for another 1 h, and finally washed with deionized water several times. A Pt foil and Ag/AgCl (3.5 M KCl) were used as counter and reference electrodes, respectively. 5 mg of carbon-supported catalyst was dispersed in 1 ml isopropanol with 20 µl of Nafion solution (5 wt%, Sigma-Aldrich), then the mixture was ultrasonicated for at least 30 min to generate a homogeneous ink. Next, 100 µl of the dispersion was transferred onto the 0.5 cm^2 carbon fiber paper, leading to a metal loading of ~ 0.2 mg cm^{-2}. All the potentials in this study were referenced to Ag/AgCl (measured) or the RHE. The potential was converted to RHE according to E (vs. RHE) = E (vs. Ag/AgCl) + 0.198 V + 0.059 × pH. Before the electrochemical measurement, the electrolyte (1 M KOH + 1 M KNO_3) was degassed by bubbling Ar for 30 min. The polarization curves were obtained by sweeping the potential from − 0.6 to -1.8 V vs. Ag/AgCl at room temperature with a sweep rate of 20 mV s^{-1}. CA measurements were conducted at different potentials for 1 h in 1 M KOH + 1 M KNO_3 solution with Ar delivered into the cathodic compartment at a rate of 20 standard cubic centimeters per minute (sccm). CV measurements taken with various scan rates (20, 40, 60 mV s^{-1}, etc.) were conducted in static solution to estimate the double-layer capacitance by sweeping the potential across the non-faradaic region − 0.1-0 V vs. Ag/AgCl. Electrochemical impedance spectroscopy measurement was performed when the working electrode was biased at a constant − 1.2 V vs. Ag/AgCl while sweeping the frequency from 100 kHz to 100 mHz with a 5 mV AC dither.

Quantification of NH_3 with Nessler's reagent. The quantity of ammonia produced was measured using a colorimetric method with Nessler's reagent. All test solutions were incubated under dark conditions at room temperature for 20 min before UV-vis tests. The absorbance at 420 nm for each solution was measured with a UV-vis spectrophotometer (Agilent N350). A series of reference solutions with suitable NH_4Cl concentrations was created to plot a calibration curve. The concentrations of ammonia in the electrolytes were obtained with this as-obtained calibration curve. The concentrations of NO_2^- was determined by Ion chromatography (Metrohm Eco IC).

Differential Electrochemical Mass Spectrometry (DEMS) measurements. DEMS was performed in a Type B cell (Hiden Analytical), using an Autolab Potentiostat (PGSTAT204, Metrohm AG). The electrocatalysts were drop-casted onto a Ti plate as the working electrode. Pt wire and Ag/AgCl were used as the counter electrode and reference electrode, respectively. 1 M KOH + 1 M KNO_3 electrolyte was kept flowing into the electrochemical cell with a flow rate of 0.5 mL min^{-1} through a peristaltic pump. Ar was bubbled into the electrolyte constantly before and during the DEMS measurements. LSV technology was employed from − 0.6 to -1.8 V vs. Ag/AgCl with a sweep rate of 20 mV s^{-1}. Mass spectra were acquired on a Hiden HPR40

(Hiden Analytical) dissolved-species mass spectrometer. An electron energy of 70 eV was used for ionization of all species, with an emission current of 450 μA. All mass-selected products were detected by a secondary electron multiplier with a detector voltage of 1200 V. After the mass signal returned to baseline at the end of the electrochemical test, the next cycle was started using the same test conditions. The experiment ended after three cycles.

In-situ attenuated total reflectance surface-enhanced infrared absorption spectroscopy (ATR-SEIRAS) experiments. ATR-SEIRAS experiments were conducted in a one-compartment PEEK spectroelectrochemical cell with the VeeMAXIII ATR accessory. A graphite rod counter electrode and a saturated Ag/AgCl reference electrode controlled by a Autolab Potentiostat (PGSTAT204, Metrohm AG) were used. IR measurements were performed in a Thermo Nicolet iS50 FTIR equipped with liquid nitrogen cooled MCT detector. A modified chemical deposition method was used to generate Au film electrodes on the reflecting plane of Si ATR crystal prisms cut to 60° incidence. The experiments were performed in 0.1 M KOH + 1 M KNO_3. 32 scans with resolution of 4 are averaged at each potential with a sampling frequency of 20 s in a CV at 5 mV/s.

DFT calculations. DFT calculations were performed using Vienna ab initio software (VASP)[44,45] with projector augmented wave psuedopotentials. The exchange correlation was treated at the GGA level using RPBE functional[46]. A planewave energy cutoff of 450 eV was used and the Methfessel-Paxton smearing scheme was used with a smearing parameter of 0.2 eV. Electronic energies are extrapolated to k_bT = 0 eV. The CuAu ordered SAA was modelled by generating (100) and (110) slabs from a *P4/mmm* ordered intermetallic CuAu bulk. The lattice constants for this bulk were optimized via DFT to be a = 2.86 Å and c = 3.66 Å. A 3 × 3 × 6 supercell with the bottom 4 layers fixed was used for the (100) slab and a 3 × 3 × 4 supercell with the bottom 2 layers fixed was used for the (110) slab. The brillouin zones for the (100) and (110) were sampled using the Monkhorst-Pack meshes of 4 × 4 × 1 and 2 × 3 × 1 respectively. An additional model system was generated to consider a compressive strain shown in Fig. 2k and Fig. 2i. The CuAu bulk was reoptimized but with the one of lattice constants compresse by 2.5 % (a = 2.79 Å), and a compressed (100) slab was generated from this bulk. The CuAu SAA was modelled by replacing a single surface Cu atom in a Cu(100) slab with Au atom. The slab was a 4 × 4 × 4 supercell with the bottom two layers fixed and the Brillouin zone was sampled using the Monkhorst-Pack mesh of 4 × 4 × 1. In order to consider the effect of the Au atom, all adsorbates were assumed to bind at a site near the Au atom. The energetics for the Cu nanocubes are the same as the values used for Cu(100) from our previous publication[35]. Grand canonical DFT calculations were performed to consider the solvation and electric field effects at the electrode/electrolyte interface. Adsorbate free formation energies were calculated similarly to our previous publication using the same corrections and references[35].

Declarations

Acknowledgements

We acknowledge the funding support from NSF CBET Catalysis (Award # 2143710). This research used resources of the Advanced Photon Source, a U.S. Department of Energy (DOE) Office of Science user facility operated for the DOE Office of Science by Argonne National Laboratory under Contract No. DE-AC02-06CH11357. Q.H. would like to acknowledge the support of the National Research Foundation (NRF) Singapore, under its NRF Fellowship (NRF-NRFF11-2019-0002), the support from the Singapore Low-carbon energy research funding initiative (Award ID LCERFI01-0017). This research used the beamline 7-BM (QAS) of the National Synchrotron Light Source II, a U.S. Department of Energy (DOE) Office of Science User Facility operated for the DOE Office of Science by the Brookhaven National Laboratory under contract no. DE-SC0012704.

These authors contributed equally to this work

Qiang Gao, Bingqing Yao and Hemanth Somarajan Pillai

Author Contributions

Q.G. and H.Z. conceptualized the project. H.Z. and H.X. supervised the project. Q.G. planned and performed the catalyst synthesis, conducted the electrocatalytic tests, collected and analysed the data. B.Y., W.Z and Q.H. collected and analysed the STEM data. H.S.P. and H.X. did the theoretical calculations. X.H., Y.L., Z.Y. and B.M. helped with synthesis of the catalysts and collected the data. S.Y. helped to perform the DEMS and ATR-SEIRAS measurements. H.Z. performed the EXAFS measurements. L.M. performed the synchrotron XRD measurements. Q.G., H.S.P., H.Z. and H.X. wrote the manuscript. All authors discussed the results and commented on the manuscript.

Competing financial interests

The authors declare no competing interests.

Additional information

Supplementary Information accompanying this paper is available at http://www.nature.com.

Correspondence and requests for materials should be addressed to H.X., Q. H., or H.Z.

References

1. van der Hoeven, J. E. S. *et al.* Unlocking synergy in bimetallic catalysts by core–shell design. Nat. Mater. **20**, 1216–1220, (2021).
2. Wu, P. *et al.* Harnessing strong metal–support interactions via a reverse route. Nat. Commun. **11**, 3042, (2020).
3. Gawande, M. B. *et al.* Core–shell nanoparticles: synthesis and applications in catalysis and electrocatalysis. Chem. Soc. Rev. **44**, 7540–7590, (2015).

4. Zhao, X. & Sasaki, K. Advanced Pt-Based Core–Shell Electrocatalysts for Fuel Cell Cathodes. Acc. Chem. Res. **55**, 1226–1236, (2022).
5. Yang, X. *et al.* Modulating Electronic Structure of an Au-Nanorod-Core–PdPt-Alloy-Shell Catalyst for Efficient Alcohol Electro-Oxidation. *Adv. Energy Mater.* **n/a**, 2100812, (2021).
6. Wang, X. *et al.* Palladium–platinum core-shell icosahedra with substantially enhanced activity and durability towards oxygen reduction. Nat. Commun. **6**, 7594, (2015).
7. Wang, H. *et al.* Significantly Enhanced Overall Water Splitting Performance by Partial Oxidation of Ir through Au Modification in Core–Shell Alloy Structure. J. Am. Chem. Soc. **143**, 4639–4645, (2021).
8. Li, M. *et al.* Exclusive Strain Effect Boosts Overall Water Splitting in PdCu/Ir Core/Shell Nanocrystals. Angew. Chem., Int. Ed. **60**, 8243–8250, (2021).
9. Zhuang, T.-T. *et al.* Steering post-C–C coupling selectivity enables high efficiency electroreduction of carbon dioxide to multi-carbon alcohols. Nat. Catal. **1**, 421–428, (2018).
10. Luc, W. *et al.* Ag–Sn Bimetallic Catalyst with a Core–Shell Structure for CO_2 Reduction. J. Am. Chem. Soc. **139**, 1885–1893, (2017).
11. Liu, C. *et al.* Favorable Core/Shell Interface within Co_2P/Pt Nanorods for Oxygen Reduction Electrocatalysis. Nano lett. **18**, 7870–7875, (2018).
12. Zhang, S. *et al.* Monodisperse Core/Shell Ni/FePt Nanoparticles and Their Conversion to Ni/Pt to Catalyze Oxygen Reduction. J. Am. Chem. Soc. **136**, 15921–15924, (2014).
13. Ji, Y. *et al.* Selective CO-to-acetate electroreduction via intermediate adsorption tuning on ordered Cu–Pd sites. Nat. Catal., (2022).
14. Yang, C.-L. *et al.* Sulfur-anchoring synthesis of platinum intermetallic nanoparticle catalysts for fuel cells. Science **374**, 459–464, (2021).
15. Wang, D. *et al.* Structurally ordered intermetallic platinum–cobalt core–shell nanoparticles with enhanced activity and stability as oxygen reduction electrocatalysts. Nat. Mater. **12**, 81–87, (2013).
16. Wang, A., Li, J. & Zhang, T. Heterogeneous single-atom catalysis. Nat. Rev. Chem. **2**, 65–81, (2018).
17. Yang, X.-F. *et al.* Single-Atom Catalysts: A New Frontier in Heterogeneous Catalysis. Acc. Chem. Res. **46**, 1740–1748, (2013).
18. Liu, J.-C., Xiao, H. & Li, J. Constructing High-Loading Single-Atom/Cluster Catalysts via an Electrochemical Potential Window Strategy. J. Am. Chem. Soc. **142**, 3375–3383, (2020).
19. Chen, Y. *et al.* Single-Atom Catalysts: Synthetic Strategies and Electrochemical Applications. Joule **2**, 1242–1264, (2018).
20. Zhang, T., Walsh, A. G., Yu, J. & Zhang, P. Single-atom alloy catalysts: structural analysis, electronic properties and catalytic activities. Chem. Soc. Rev. **50**, 569–588, (2021).
21. Kaiser, S. K., Chen, Z., Faust Akl, D., Mitchell, S. & Pérez-Ramírez, J. Single-Atom Catalysts across the Periodic Table. Chem. Rev. **120**, 11703–11809, (2020).
22. Hannagan, R. T., Giannakakis, G., Flytzani-Stephanopoulos, M. & Sykes, E. C. H. Single-Atom Alloy Catalysis. Chem. Rev., (2020).

23. Han, A. *et al.* Isolating contiguous Pt atoms and forming Pt-Zn intermetallic nanoparticles to regulate selectivity in 4-nitrophenylacetylene hydrogenation. Nat. Commun. **10**, 3787, (2019).
24. Feng, Q. *et al.* Isolated Single-Atom Pd Sites in Intermetallic Nanostructures: High Catalytic Selectivity for Semihydrogenation of Alkynes. J. Am. Chem. Soc. **139**, 7294–7301, (2017).
25. Armbrüster, M. *et al.* $Al_{13}Fe_4$ as a low-cost alternative for palladium in heterogeneous hydrogenation. Nat. Mater. **11**, 690–693, (2012).
26. Nakaya, Y., Hirayama, J., Yamazoe, S., Shimizu, K.-i. & Furukawa, S. Single-atom Pt in intermetallics as an ultrastable and selective catalyst for propane dehydrogenation. Nat. Commun. **11**, 2838, (2020).
27. Xia, X. H., Wang, Y., Ruditskiy, A. & Xia, Y. N. 25th Anniversary Article: Galvanic Replacement: A Simple and Versatile Route to Hollow Nanostructures with Tunable and Well-Controlled Properties. Adv. Mater. **25**, 6313–6333, (2013).
28. González, E., Arbiol, J. & Puntes, V. F. Carving at the Nanoscale: Sequential Galvanic Exchange and Kirkendall Growth at Room Temperature. Science **334**, 1377–1380, (2011).
29. Chen, F.-Y. *et al.* Efficient conversion of low-concentration nitrate sources into ammonia on a Ru-dispersed Cu nanowire electrocatalyst. Nat. Nanotechnol., (2022).
30. Wang, Y., Wang, C., Li, M., Yu, Y. & Zhang, B. Nitrate electroreduction: mechanism insight, in situ characterization, performance evaluation, and challenges. Chem. Soc. Rev. **50**, 6720–6733, (2021).
31. Min, B. *et al.* Powering the Remediation of the Nitrogen Cycle: Progress and Perspectives of Electrochemical Nitrate Reduction. Ind. Eng. Chem. Res. **60**, 14635–14650, (2021).
32. Rosca, V., Duca, M., de Groot, M. T. & Koper, M. T. M. Nitrogen Cycle Electrocatalysis. Chem. Rev. **109**, 2209–2244, (2009).
33. Guo, H. *et al.* Shape-Selective Formation of Monodisperse Copper Nanospheres and Nanocubes via Disproportionation Reaction Route and Their Optical Properties. J. Phys. Chem. C **118**, 9801–9808, (2014).
34. Zhao, J., Chen, B. & Wang, F. Shedding Light on the Role of Misfit Strain in Controlling Core–Shell Nanocrystals. Adv. Mater. **32**, 2004142, (2020).
35. Gao, Q. *et al.* Breaking adsorption-energy scaling limitations of electrocatalytic nitrate reduction on intermetallic CuPd nanocubes by machine-learned insights. Nat. Commun. **13**, 2338, (2022).
36. Wu, Z.-Y. *et al.* Electrochemical ammonia synthesis via nitrate reduction on Fe single atom catalyst. Nat. Commun. **12**, 2870, (2021).
37. Wang, Y., Zhou, W., Jia, R., Yu, Y. & Zhang, B. Unveiling the Activity Origin of a Copper-based Electrocatalyst for Selective Nitrate Reduction to Ammonia. Angew. Chem., Int. Ed. **59**, 5350–5354, (2020).
38. Wang, Y. *et al.* Enhanced nitrate-to-ammonia activity on copper-nickel alloys via tuning of intermediate adsorption. J. Am. Chem. Soc. **142**, 5702–5708, (2020).

39. Li, J. *et al.* Efficient Ammonia Electrosynthesis from Nitrate on Strained Ruthenium Nanoclusters. J. Am. Chem. Soc. **142**, 7036–7046, (2020).
40. Yao, Y., Zhu, S., Wang, H., Li, H. & Shao, M. A Spectroscopic Study on the Nitrogen Electrochemical Reduction Reaction on Gold and Platinum Surfaces. J. Am. Chem. Soc. **140**, 1496–1501, (2018).
41. da Cunha, M. C. P. M., De Souza, J. P. I. & Nart, F. C. Reaction Pathways for Reduction of Nitrate Ions on Platinum, Rhodium, and Platinum – Rhodium Alloy Electrodes. Langmuir **16**, 771–777, (2000).
42. Yao, Y., Zhu, S., Wang, H., Li, H. & Shao, M. A Spectroscopic Study of Electrochemical Nitrogen and Nitrate Reduction on Rhodium Surfaces. Angew. Chem., Int. Ed. **59**, 10479–10483, (2020).
43. Dovgolevsky, E. & Haick, H. Direct Observation of the Transition Point Between Quasi-Spherical and Cubic Nanoparticles in a Two-Step Seed-Mediated Growth Method. Small **4**, 2059–2066, (2008).
44. Kresse, G. & Furthmüller, J. Efficiency of ab-initio total energy calculations for metals and semiconductors using a plane-wave basis set. Comput. Mater. Sci. **6**, 15–50, (1996).
45. Kresse, G. & Furthmüller, J. Efficient iterative schemes for ab initio total-energy calculations using a plane-wave basis set. Phys. Rev. B **54**, 11169–11186, (1996).
46. Hammer, B., Hansen, L. B. & Nørskov, J. K. Improved adsorption energetics within density-functional theory using revised Perdew-Burke-Ernzerhof functionals. Phys. Rev. B **59**, 7413–7421, (1999).

Figures

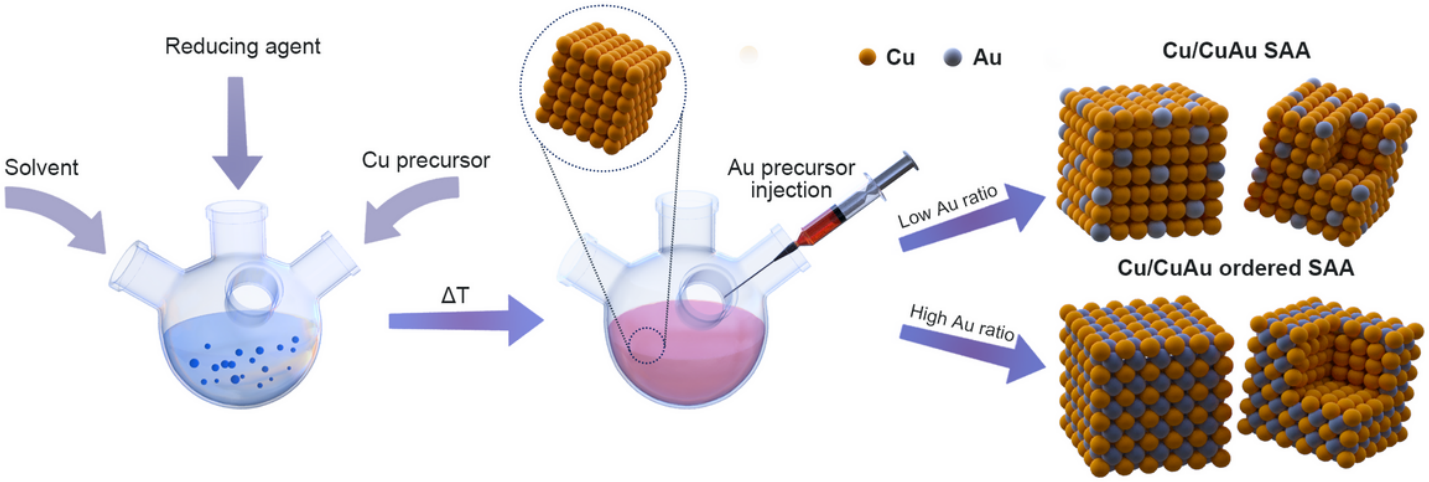

Figure 1

Schematic illustration of the core/shell Cu/CuAu SAA synthesis. Colloidal synthesis with Cu nanocubes forms first as seeds for the subsequent deposition of CuAu SAA on Cu through galvanic replacement.

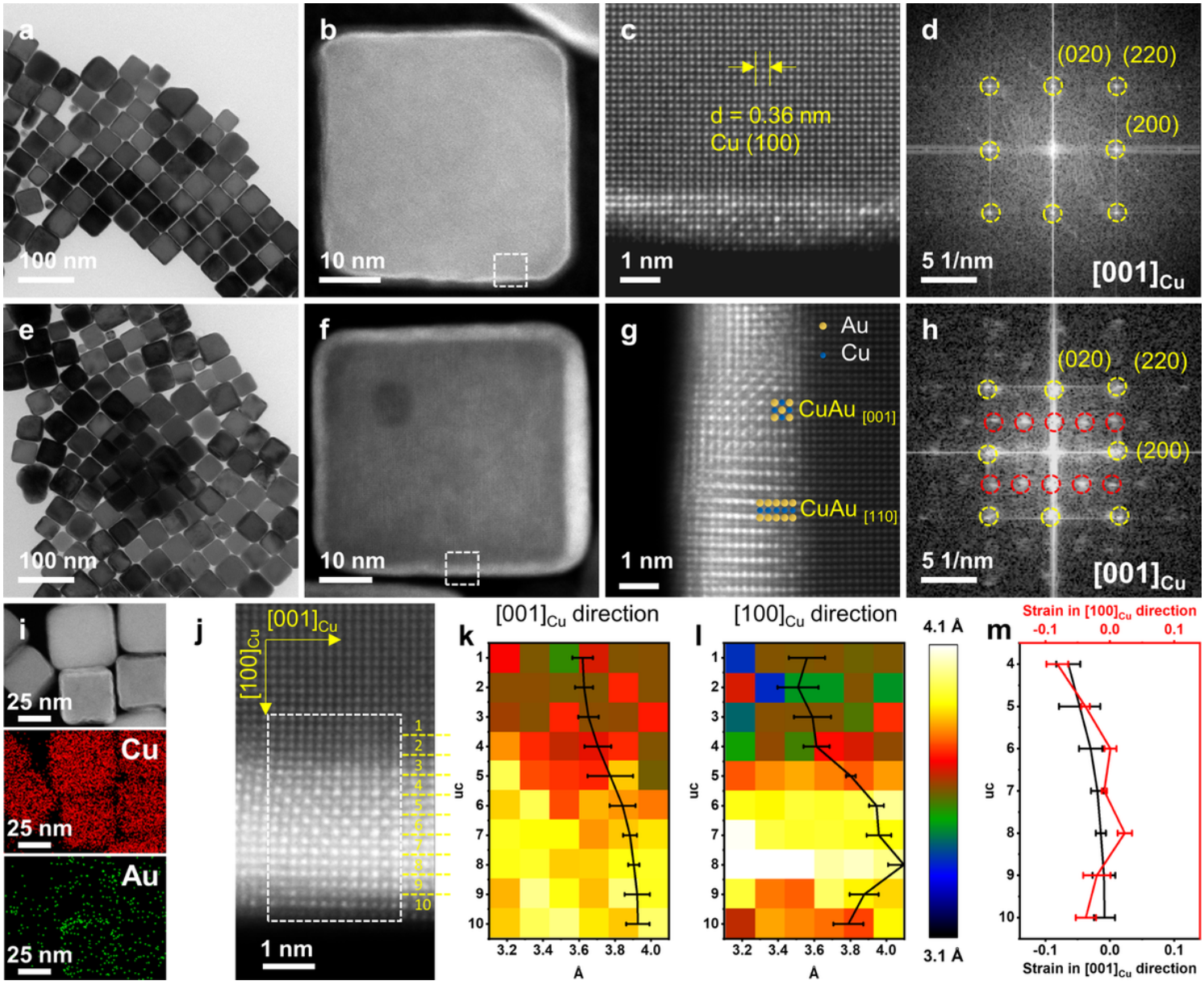

Figure 2

Characterizations of core/shell Cu/CuAu SAA nanocubes. a, BF-TEM, **b**, HAADF-STEM **c**, atomic-resolution HAADF-STEM images, and**d**, the corresponding FFT pattern of Cu/CuAu SAA nanocubes. **e**, BF-TEM, **f**, HAADF-STEM **g**, atomic-resolution HAADF-STEM images, and **h**, the corresponding FFT pattern of Cu/CuAu ordered SAA nanocubes. (c) and (g) are zoomed views from area highlighted with dash lines in (b) and (f), respectively, showing the atomic-resolved shell structure from the [001] direction. The red dashed circles in (h) indicate the superlattice reflections' characteristic of the CuAu ordered structure compared to (d). **i**, HAADF-STEM image, and Au and Cu elemental maps of Cu/CuAu ordered SAA nanocubes. **j**, HAADF-STEM images, **k**, **l**, the corresponding unit cell mapping and **m**, strain profile of Cu/CuAu ordered SAA nanocubes. (k-l) were calculated from the area highlighted with dash lines in (j).

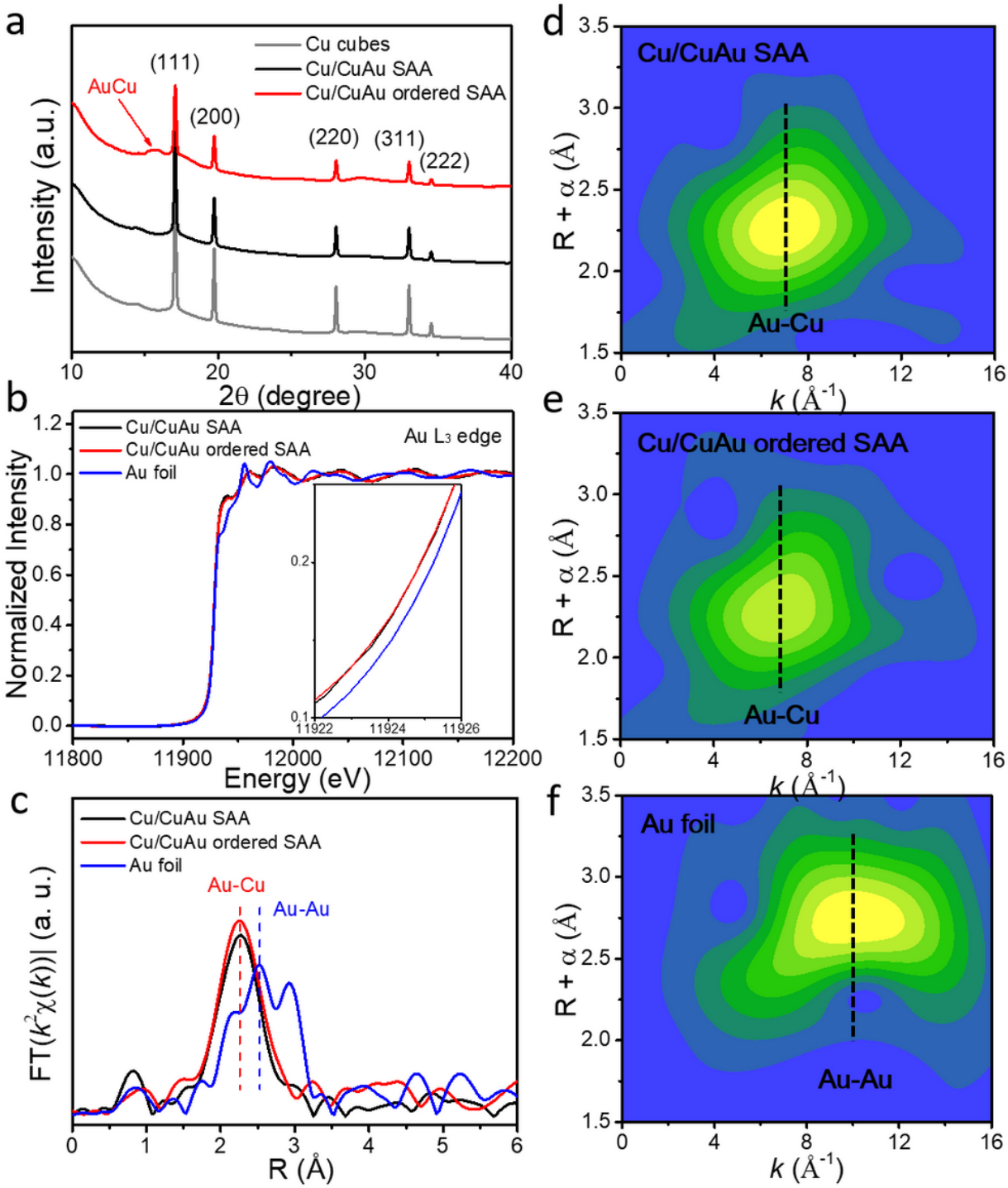

Figure 3

Structural characterizations of the Cu/CuAu SAA nanocubes. a, synchrotron XRD patterns of Cu/CuAu SAA, Cu/CuAu ordered SAA nanocubes, and Cu nanocubes. **b**, Au L3-edge XANES spectra of Cu/CuAu SAA, Cu/CuAu ordered SAA nanocubes, and Au foil reference, with a zoomed view of the Au L3-edge as inset. **c**, EXAFS Fourier transformed k2-weighted χ(k) function spectra of Cu/CuAu SAA, Cu/CuAu ordered SAA nanocubes, and Au foil reference. **d**, **e**, **f**, Au L3-edge WT EXAFS of Cu/CuAu SAA, Cu/CuAu ordered SAAnanocubes, and Au foil reference.

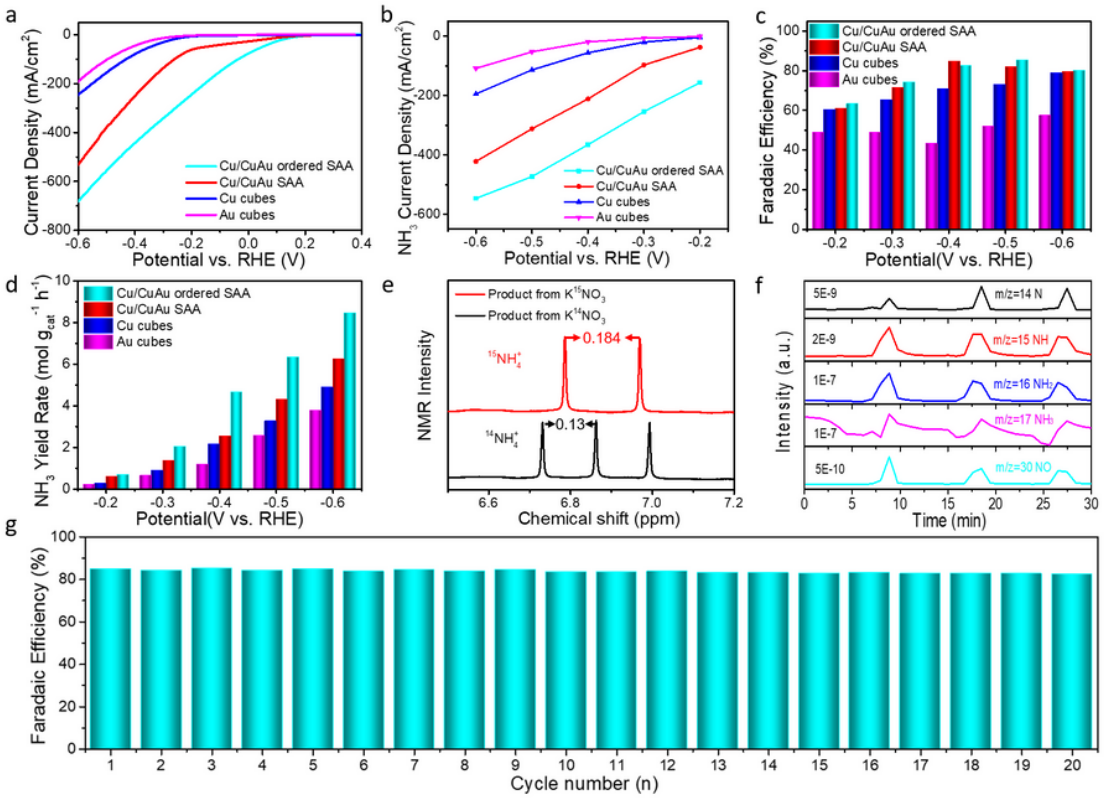

Figure 4

Electrocatalytic NO3RR performance of the Cu/CuAu ordered SAA nanocubes. a, linear scan voltammetry curves of Cu/CuAu ordered SAA nanocubes, Cu/CuAu SAA nanocubes, Cu nanocubes, and Au nanocubes normalized to the geometric area. **b**, partial NH3 current densities normalized to the geometric area. **c**, FE of NH3 at different potentials. **d**, NH3 yield rates at various potentials. **e**, NMR spectrum of the products generated during the electrocatalytic NO3RR with Cu/CuAu ordered SAA nanocubes in 1 M K15NO3 or 1 M K14NO3at -0.6 V vs. RHE. **f**, the online DEMS measurements of NO3RR on Cu/CuAu ordered SAA. **g**, stability test by running 20 consecutive electrolysis cycles on Cu/CuAu ordered SAA nanocubes at -0.5 V vs. RHE.

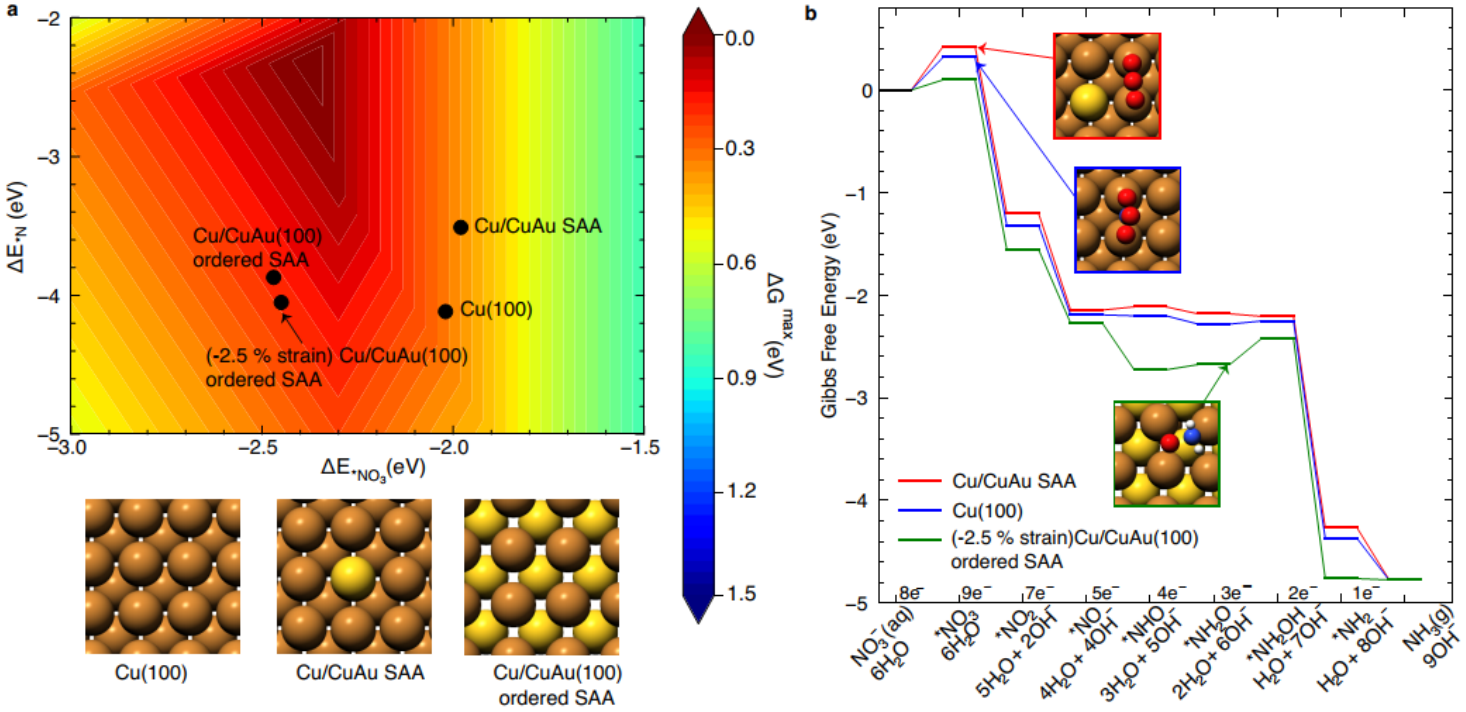

Figure 5

NO3RR reaction pathway and activity map. a, Activity volcano plot of NO3RR to NH3 using the binding energies of *NO3 and *N as descriptors with (100)-terminated Cu(100), Cu/CuAu(100) SAA, and Cu/CuAu(100) ordered SAA with and without surface strains overlaid on the map. Structural models used in DFT calculations are shown. **b**, Free energy pathways of nitrate reduction on Cu(100), strained ordered Cu/CuAu(100) SAA, and Cu/CuAu SAA.

Supplementary Files

This is a list of supplementary files associated with this preprint. Click to download.

- CuAuSAANO3RRSI.docx